Astronomy & Astrophysics manuscript no. Herm33es˙3d
May 20, 2010
© ESO 2010

arXiv:1005.3422v1 [astro-ph.CO] 19 May 2010

Letter to the Editor

Cool gas and dust in M33: Results from the *Herschel* M33 extended survey (HERM33ES). ⋆

J. Braine[1], P. Gratier[1], C. Kramer[2], E.M. Xilouris[3] E. Rosolowsky[4], C. Buchbender[2], M. Boquien[5], D. Calzetti[5], G. Quintana-Lacaci[2], F. Tabatabaei[6], S. Verley[7], F. Israel[8], F. van der Tak[9], S. Aalto[10], F. Combes[11], S. Garcia-Burillo[12], M. Gonzalez[2], C. Henkel[6], B. Koribalski[13], B. Mookerjea[14], M. Roellig[15], K.F. Schuster[16], M. Relaño[18], F. Bertoldi[19], P. van der Werf[8], and M. Wiedner[11]

(Affiliations can be found after the references)

Received / Accepted 11 May, 2010

ABSTRACT

We present an analysis of the first space-based far-IR-submm observations of M 33, which measure the emission from the cool dust and resolve the giant molecular cloud complexes. With roughly half-solar abundances, M33 is a first step towards young low-metallicity galaxies where the submm may be able to provide an alternative to CO mapping to measure their H_2 content. In this Letter, we measure the dust emission cross-section σ using SPIRE and recent CO and H I observations; a variation in σ is present from a near-solar neighborhood cross-section to about half-solar with the maximum being south of the nucleus. Calculating the total H column density from the measured dust temperature and cross-section, and then subtracting the H I column, yields a morphology similar to that observed in CO. The H_2/H I mass ratio decreases from about unity to well below 10% and is about 15% averaged over the optical disk. The single most important observation to reduce the potentially large systematic errors is to complete the CO mapping of M 33.

Key words. Galaxies: Individual: M 33 – Galaxies: Local Group – Galaxies: evolution – Galaxies: ISM – ISM: Clouds – Stars: Formation

1. Introduction, data, and dust temperature

Understanding star formation requires studying the interplay between the phases of the interstellar medium (ISM). Dust processes most of the energy transiting the ISM, but the cool dust component, although representing the vast majority of the dust mass, is difficult to observe from the ground. *Herschel* SPIRE observations (Pilbratt 2010; Griffin 2010) are the first space-based 250-500 μm data and as such provide a unique occasion to put together a global picture of the cool gas and dust in M 33. In particular, we compare the morphology of the Far-IR emission and that of the gas as determined from CO and H I measurements and attempt to measure how the dust cross-section varies in M 33. A longer term goal is to be able to use the dust emission to constrain the variation of the $N(H_2)/I_{CO}$ factor within M 33 and elsewhere.

This Letter is one of a series on the `HERM33ES` project on the ISM of the Local Group galaxy M 33, an overview of which is given in Kramer et al. (2010), hereafter K10. For consistency with the other M 33 papers in this volume, we adopt a distance of $D = 840$ kpc for M 33 (i.e., 25 arcsec = 100 pc) and orientation parameters of $PA = 22.5$ degrees and $i = 56°$. We use the recent `HERM33ES` SPIRE observations at 250, 350, and 500 μm combined with CO(2–1) observations from the M33CO@IRAM project, as a tracer of the molecular component, and a high-resolution mosaic of VLA HI data (both from Gratier et al. 2010). The SPIRE data were first processed as described in K10 and then converted from Jy/beam to brightness units (MJy/sr). To estimate the dust temperature, the 250μm data were convolved to the 350μm beamsize ($\sim$ 25") and, assuming a single temperature grey body with an emissivity $\propto \nu^\beta$ with $\beta = 2$, a temperature was derived from the flux ratio. At the temperatures of the cool component seen in M 33, Dupac et al. (2003) find $\beta \approx 2$. To minimize the effect of the uncertainty in β, we chose to use adjacent bands to estimate temperature. The 250/350μm ratio provides more accurate temperatures than the 350/500 micron ratio even for temperatures below 10 K. A 15% variation (or uncertainty) in the 250/350μm ratios corresponds to a temperature change of 0.9, 2.1, and 4.1 K at temperatures of 10, 15, and 20 K but the same uncertainty in the 350/500μm ratios yields 1.3, 3.2, and 6.3 K errors for the same dust temperatures. A further advantage is that we obtain the dust temperature at a resolution typical of giant molecular clouds (GMC), $\sim$ 100 pc.

Ideally, a multi-component fit would be used but this requires high S/N data at many wavelengths over the whole disk. By assuming that the cool dust component dominates the emission beyond 250μm, we could calculate the dust temperature out to the optical radius of M 33. The resulting temperature map is shown in Fig. 1. Figure 2 shows a comparison with the temperature of the cool component of the preferred two-component (warm plus cool

Send offprint requests to: J. Braine, e-mail: `Braine@obs.u-bordeaux1.fr`

⋆ *Herschel* is an ESA space observatory with science instruments provided by European-led Principal Investigator consortia and with important participation from NASA.

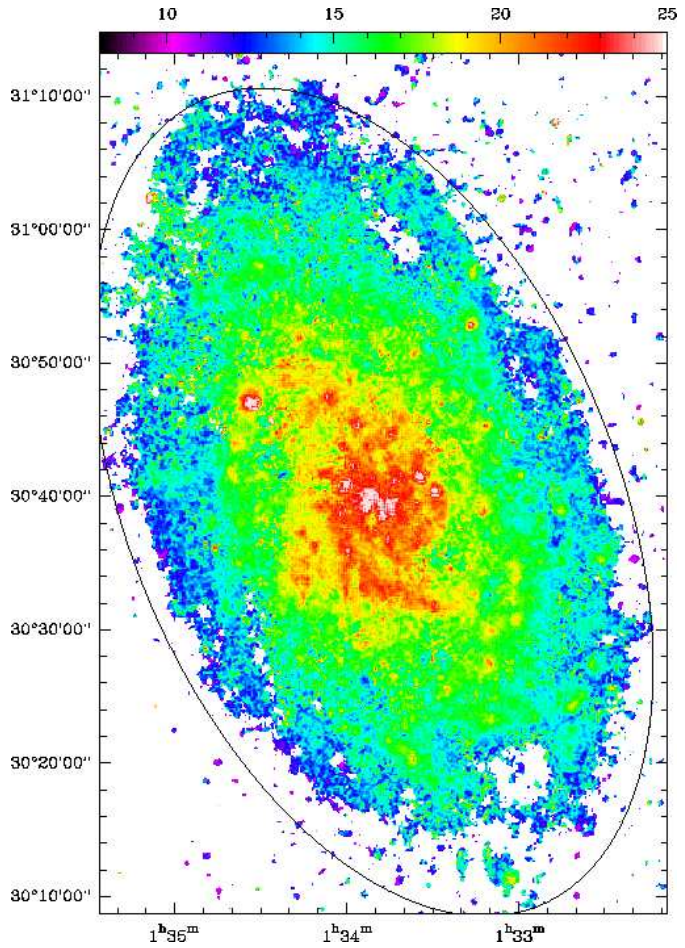


Fig. 1. Dust color temperature map of M 33 calculated from the SPIRE 250 and 350 μm flux ratio with $\beta = 2$ at the $\sim 25''$ resolution of the 350μm data. Coordinates are J2000, the temperature scale is shown at the top in Kelvin, and the ellipse shows the 8 kpc radius, slightly beyond R_{25}.

dust) model fit to data between 24μm and 500μm from K10. The two-component model uses $\beta = 1.5$ and the temperatures are higher out to 6 kpc. The temperatures in the radial bins have been estimated by averaging the temperatures rather than averaging the emission as in K10. The latter yields slightly higher temperatures because the dust is usually warmer where emission is strong (compare Fig. 1 with Fig 1. in K10). K10 calculate the dust column density using $\kappa = 0.4(\nu/250\mathrm{GHz})^2$ cm^2g^{-1} of dust, which is equivalent to a dust cross-section per H-atom of $\sigma = 1.1 \times 10^{-25}(\lambda/250\mu\mathrm{m})^{-2}\mathrm{cm}^2$ for a hydrogen gas-to-dust mass ratio of 140. In the following we use the SPIRE 250/350 μm color temperature because the data cover a greater area and agree well with the cool dust temperature of the two-component fit, showing the domination of the cool dust at these wavelengths. No correction for line contamination was subtracted from the SPIRE data. At these frequencies, the CO lines contribute very little to the continuum flux, unlike at 1.3mm or 850μm (e.g. Braine et al. 1997).

Figure 3 shows the SPIRE 250μm emission with the CO(2–1) emission as contours at $25''$ resolution to show how closely the CO emission follows the dust emission peaks. Gratier et al. (2010) show a detailed comparison of the CO and H I emission with star formation tracers such as Hα and *Spitzer* 8 and 24μm maps. The 250μm-bright regions are detected in CO and the general morphology of the cool dust emission is seen in the H I image.

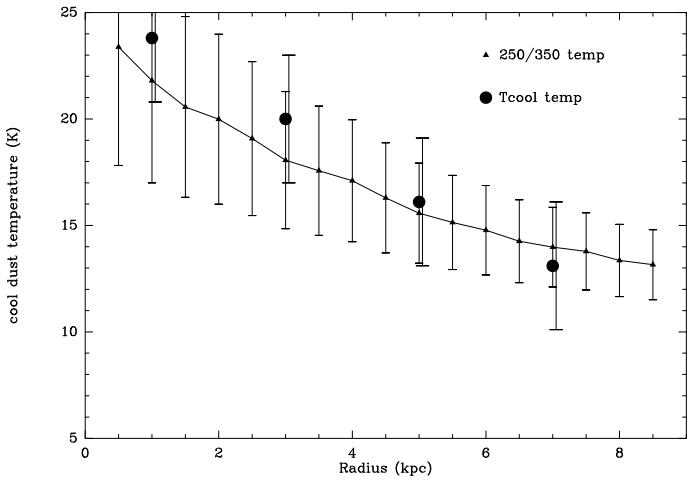


Fig. 2. Radial distribution of the average dust temperature in the stellar disk of M 33. The solid line joining the triangles shows the 250/350 μm color temperature and for comparison we show the cool dust temperature (large dots) obtained by K10 in their preferred two-component model with $\beta = 1.5$. The error bars on the triangles indicate a 15% calibration uncertainty in the 250/350 μm ratio converted to temperature.

2. Dust cross-section

In order to estimate the total gas mass of a galaxy from its dust emission, it is first necessary to measure the dust emission cross-section per H-atom σ. We do this by selecting regions with HI emission and well-constrained dust temperatures but with little or no CO emission (in order to avoid the assumption of a $N(\mathrm{H}_2)/I_{\mathrm{CO}}$ value and CO line ratio). Thereby, we can relate the observed neutral hydrogen column density, $\mathrm{N_{HI}}$, to the dust optical depth, $\tau = \sigma \mathrm{N_H} = S_\nu/B_{\nu,T}$, and infer the cross section σ. In practice, two methods were used: (*i*) we selected large contiguous regions as shown on the map in Fig. 3 and (*ii*) all pixels with HI emission, a defined dust temperature, and no detected CO emission ($\mathrm{I_{co}} < 0.05$ K km s^{-1}) were taken, using maps at the resolution of the 350μm SPIRE data. In the optically thin limit,

$$N_{\mathrm{tot}} = N_{\mathrm{HI}} + N_{\mathrm{H_2}} = S_\nu/(\sigma\ B_{\nu,T}) \quad (1)$$

where S_ν is the flux density and N_{tot} is the H column density. Where CO is not detected (i.e. $N_{\mathrm{tot}} \approx N_{\mathrm{HI}}$), we can calculate σ from the dust temperature and the observed H I column density and SPIRE flux by $\sigma \approx S_\nu/(N_{\mathrm{HI}}\ B_{\nu,T})$.

From the regions indicated in Fig. 3, we estimate σ (using Eq. 1) for different radii and the results are shown in the first line of Table 1. We assume that the cross section within the inner 4 kpc is the same as at 4kpc for two reasons: (*i*) there are few truly CO-free regions in the central part of M 33 and (*ii*) Gardan et al. (2007) showed (their Fig. 13) that the H I-H_2 relation was similar within 4kpc

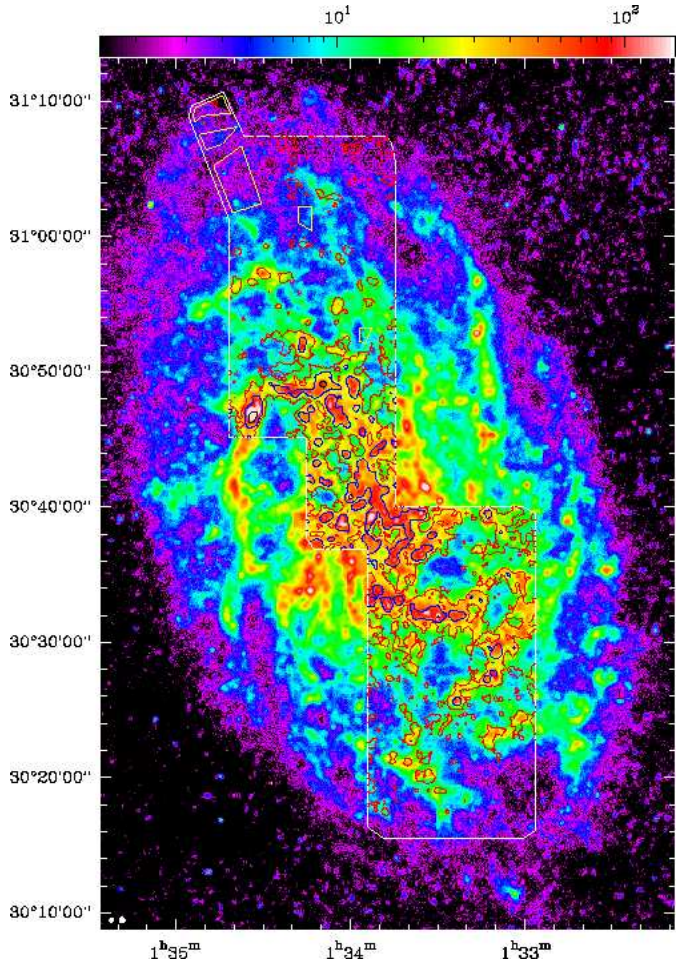


Fig. 3. SPIRE 250μm emission with the IRAM CO(2–1) emission at 25″ resolution superposed as contours and with the polygons to the upper left used to calculate the dust cross-section per H-atom. The beams are shown as white dots in the lower left corner. The CO contours are at 0.5 (red), 2 (blue), and 4 K km s^{-1} in the main beam scale. The large polygon indicates the area covered so far by the IRAM CO survey.

but beyond 4 kpc the H_2 fraction decreased sharply even at constant total Hydrogen column density, so we consider $R \sim 4$kpc as a transition in ISM properties. It is very likely that some molecular gas is present in these regions, particularly those closer to the center, so σ is likely overestimated. In the second approach, in order to exclude averaging in undetected molecular clouds, we take the peak of the histogram of σ values for the areas without detected CO emission but with HI emission and a constrained dust temperature, yielding the lower values for σ, as shown in Table 1. Using this method, we find a north-south difference in M33 at equivalent radii. The uncertainty in the histogram method is about ± 0.1; although the distribution is sometimes broad, the peak value is well defined. The histograms of σ values are clearly different in the north and south. The polygon method was difficult to use in the south due to the absence of large CO-free regions with HI and dust emission. An advantage of the histogram method is that it excludes the tail of high σ which may be due to H_2 without detected CO emission.

The intrinsic expectation is that because the oxygen abundance is about half solar, the dust cross-section should be as well (Draine et al. 2007), and that given the shallow abundance gradient in M33 (Rosolowsky et al. 2007; Magrini et al. 2009), this should hold for the entire galaxy. However, it quickly became apparent that the dust cross-section per H-atom varied over the galaxy, decreasing with radius by close to a factor 2, with a higher abundance in the south – similar to the variation found by Magrini et al. (2010) from optical H II region and PNe abundance measurements. In the solar neighborhood, σ is about $\sigma \approx 1.1 \times 10^{-25}$cm^2 per H-atom (Draine & Lee 1984; Draine & Li 2007) at 250μm and varying as ν^2. If we apply a σ of half this value to M33 using the dust temperature map in Fig. 1, we obtain unrealistically high gas masses in the inner disk: ~ 40 M$_\odot$ pc^{-2} on average, whereas the H I is about 11 M$_\odot$ pc^{-2} and the H_2 considerably less (Gratier et al. 2010). For a half-solar σ, the (cool) dust temperature would have to be about 30K, beyond any experimental uncertainties, so we conclude that σ must be higher in the inner disk. In the outer disk, however, the H I column density (where no CO emission is present) is roughly equal to what is derived from the dust with $\sigma = 0.5\sigma_\odot$, suggesting that this value is appropriate for the outer disk.

Table 1. Dust cross-section σ at 250μm as a function of radius in M33, expressed in units of 1.1×10^{-25}cm^2 per H-atom. The polygons are shown in Fig. 3. The histogram method was applied separately in the north and south (lines 2 and 3), leading to the "Model" values used to estimate the total H column density to make Fig. 4.

r (kpc)	4	5	5.5	6	7	7.5
Polygons	1.8	1.02	..	1.07	0.66	0.50
histo-N	0.65	..	0.54	..	..	0.48
histo-S	0.92	..	0.95	0.69	..	..
Model	0.8	..	0.75	..	0.66	0.5

3. Total and molecular gas mass

To really obtain an accurate gas mass from the cold dust emission data, the calibration uncertainties in the SPIRE bands must be reduced because the 15% uncertainty is not sufficient to distinguish between different solutions of β and temperature. A second requirement is that the whole disk of M33 must be observed in CO so that a well-determined variation of σ, based on the second technique, can be constructed. The H I data provide a reliable picture of the H I column density, so subtracting this from the total gas column density derived from the dust emission yields an estimate of the molecular gas mass which does not rely on CO emission. A further caveat is that σ must not change from the atomic to molecular medium. Once the [C I] and [C II] lines have been measured, these uncertainties can be reduced by the additional constraint that the C/H ratio (from the sum of the C reservoirs) should be equal to the C abundance derived by other means.

Using the information currently available, we have used Table 1 (second method) to build an image of the dust cross-section σ, erring on the low-σ side, as indicated in the last line of Table 1. We then used this σ, scaled to 500μm with $\beta = 2$, and the dust temperature (Fig. 1) to estimate

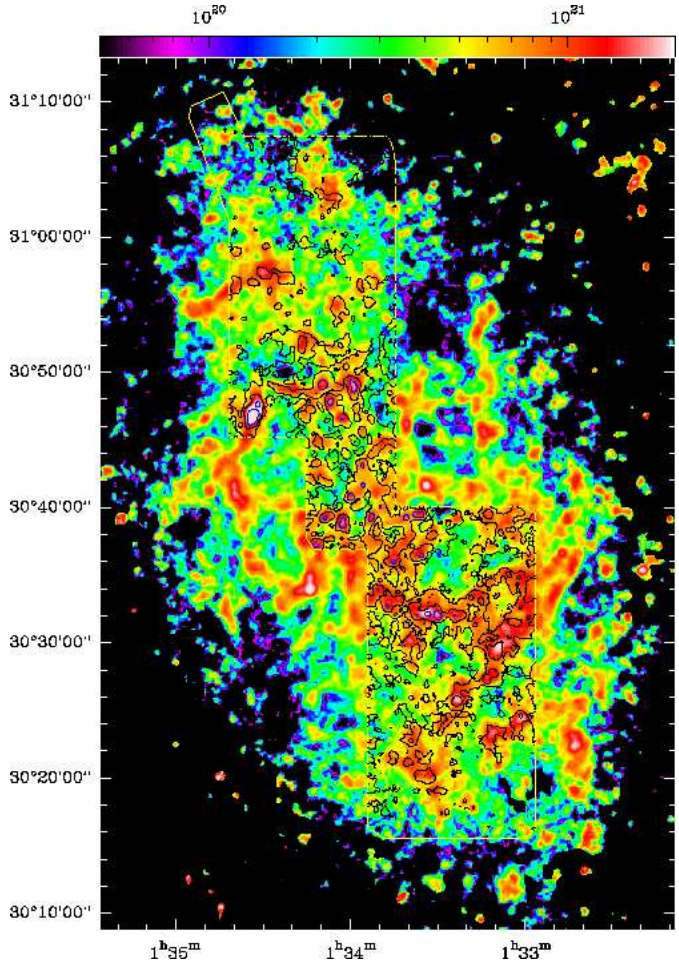


Fig. 4. H_2 column density map estimated from the 500μm SPIRE map, $\beta = 2$, the 250/350μm dust temperature as shown in Fig. 1, the H I data from Gratier et al. (2010), and the cross-sections given in Table 1. The column density scale is shown at the top in units of H_2 molecules per cm^2. CO contours at 0.4 and 1.6 K km/s (black) and 5 K km/s (blue) are superposed.

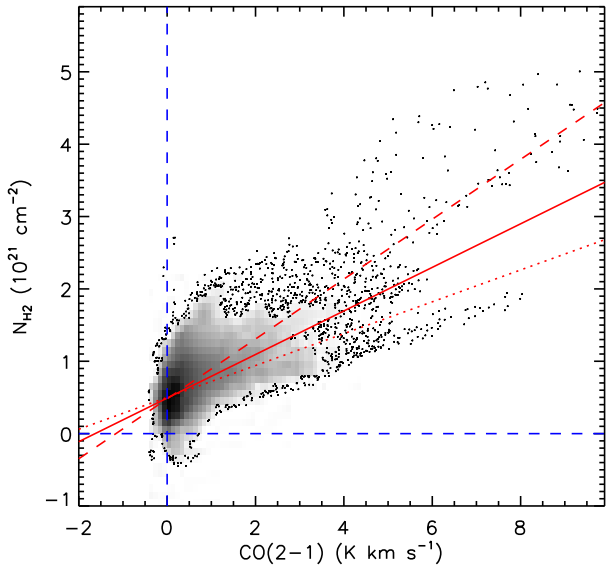


Fig. 5. Scatter plot of H_2 column density as derived from the dust emission and the CO(2-1) intensity. The solid red line is a fit to the entire dataset and corresponds to a $N(H_2)/I_{CO(2-1)}$ value of 3×10^{20} H_2 per K km s^{-1} with an offset as described in the text. A radial variation is present: fitting within 2 kpc yields a $N(H_2)/I_{CO(2-1)}$ value of 2.2×10^{20} H_2 per K km s^{-1} and 4.1×10^{20} H_2 per K km s^{-1} beyond 2 kpc (dotted and dashed lines, respectively).

the total gas mass from the 500μm data and then subtracted the H I column density to obtain the H_2 column density using the interferometric H I maps from Gratier et al. (2010), which recover more than 90% of the flux found by Putman et al. (2009) using Arecibo. The missing 21cm flux is expected to be located in the mid-to-outer disk where the rotation curve is fairly flat. A morphological comparison of the dust-derived H_2 column and the CO contours in Fig. 4 shows that while major regions were not missed by the CO observations, the dust-derived H_2 map does not correlate perfectly with the CO. For example, the strong CO peak at ($01^h34^m09^s.4$,+30°49′06″) corresponds to a red (not white) region in Fig. 4; this may of course reflect a real variation in the $N(H_2)/I_{CO}$ ratio.

The data used in the scatter plot in Fig. 5 (see also Fig. 7 in Leroy et al. 2009) yield a formal fit with a $N(H_2)/I_{CO(2-1)} = 3 \times 10^{20}$ H_2 per K km s^{-1} value, corresponding to a roughly galactic $N(H_2)/I_{CO(1-0)} = 2.1 \times 10^{20}$ H_2 per K km s^{-1} for a line ratio CO($\frac{2-1}{1-0}$) = 0.7. The inner disk $N(H_2)/I_{CO(2-1)}$ is lower and rises to about 4×10^{20} H_2 per K km s^{-1} beyond 2 kpc. The offset, in principle, implies that some low column density H_2 is not seen in CO. Both values depend strongly on the details of the dust cross-section, illustrating the need for a complete map of M 33 in CO.

The total hydrogen mass derived from the dust emission within 8kpc is estimated to be 1.63×10^9 M$_\odot$, very similar to the more directly measured H I+H_2 masses in Gratier et al. (2010). The dust cross-sections we derive suggest dust-to-gas mass ratios (including He) ranging from $\sim$ 125 in the inner 4 kpc to 200 near R_{25} for Milky Way like dust (*cf.* K10). Comparing the total dust-derived H_2 mass with the CO luminosity (Gratier et al. 2010) yields a $N(H_2)/I_{CO}$ of about 1.5 times the Galactic $N(H_2)/I_{CO}$. Because the H I dominates, however, a small error in the total dust-derived gas mass translates into a large uncertainty in the dust-derived H_2 mass. It is clearly necessary to obtain whole-galaxy measurements of σ in CO-free zones to refine these estimates.

References

Braine, J., Guélin, M., Dumke, M., et al. 1997, A&A, 326, 963
Draine, B. T., Dale, D. A., Bendo, G., et al. 2007, ApJ, 663, 866
Draine, B. T. & Lee, H. M. 1984, ApJ, 285, 89
Draine, B. T. & Li, A. 2007, ApJ, 657, 810
Dupac, X., Bernard, J., Boudet, N., et al. 2003, A&A, 404, L11
Gardan, E., Braine, J., Schuster, K. F., Brouillet, N., & Sievers, A. 2007, A&A, 473, 91
Gratier, P., Braine, J., Rodriguez-Fernandez, N. J., et al. 2010, ArXiv e-print 1003.3222
Griffin, M. e. a. 2010, A&A, this, volume
Kramer, C., Buchbender, C., Xilouris, E., et al. 2010, A&A, this, volume
Leroy, A. K., Bolatto, A., Bot, C., et al. 2009, ApJ, 702, 352

Magrini, L., Stanghellini, L., Corbelli, E., Galli, D., & Villaver, E. 2010, A&A, 512, 63
Magrini, L., Stanghellini, L., & Villaver, E. 2009, ApJ, 696, 729
Pilbratt, G. e. a. 2010, A&A, this, volume
Putman, M. E., Peek, J. E. G., Muratov, A., et al. 2009, ApJ, 703, 1486
Rosolowsky, E., Keto, E., Matsushita, S., & Willner, S. P. 2007, ApJ, 661, 830

[1] Laboratoire d'Astrophysique de Bordeaux, Université Bordeaux 1, Observatoire de Bordeaux, OASU, UMR 5804, CNRS/INSU, B.P. 89, Floirac F-33270
[2] Instituto Radioastronomia Milimetrica (IRAM), Av. Divina Pastora 7, Nucleo Central, E-18012 Granada, Spain
[3] Institute of Astronomy and Astrophysics, National Observatory of Athens, P. Penteli, 15236 Athens, Greece
[4] University of British Columbia, Okanagan, 3333 University Way, Kelowna BC V1V 1V7 Canada
[5] Department of Astronomy, University of Massachusetts, Amherst, MA 01003, USA
[6] Max-Planck-Institut für Radioastronomie (MPIfR), Auf dem Hügel 69, D-53121 Bonn, Germany Argelander Institut fr Astronomie. Auf dem Hügel 71, D-53121 Bonn, Germany
[7] Dept. Física Teórica y del Cosmos, Universidad de Granada, Spain
[8] Leiden Observatory, Leiden University, PO Box 9513, NL 2300 RA Leiden, The Netherlands
[9] SRON Netherlands Institute for Space Research, Landleven 12, 9747 AD Groningen, The Netherlands
[10] Onsala Space Observatory, Chalmers University of Technology, 43992 Onsala, Sweden
[11] Observatoire de Paris, LERMA, 61 Av. de l'Observatoire, 75014 Paris, France
[12] Observatorio Astronómico Nacional (OAN) - Observatorio de Madrid, Alfonso XII 3, 28014 Madrid, Spain
[13] Australia Telescope National Facility, CSIRO, PO Box 76, Epping, NSW 1710, Australia
[14] Department of Astronomy & Astrophysics, Tata Institute of Fundamental Research, Homi Bhabha Road, Mumbai 400005, India
[15] KOSMA, I. Physikalisches Institut, Universität zu Köln, Zülpicher Straße 77, D-50937 Köln, Germany
[16] IRAM, 300 rue de la Piscine, 38406 St. Martin d'Hères, France
[17] Institute of Astronomy, University of Cambridge, Madingley Road, Cambridge CB3 0HA, England
[18] Argelander Institut fr Astronomie. Auf dem Hügel 71, D-53121 Bonn, Germany